

In-situ SEM investigation on the damage behavior of an interpenetrating metal ceramic composite

Philipp Christopher Morbitzer, Joél Schukraft, Christoph Lohr, Kay André Weidenmann

Angaben zur Veröffentlichung / Publication details:

Morbitzer, Philipp Christopher, Joél Schukraft, Christoph Lohr, and Kay André Weidenmann. 2023. "In-situ SEM investigation on the damage behavior of an interpenetrating metal ceramic composite." *Composite Structures* 321: 117278. <https://doi.org/10.1016/j.compstruct.2023.117278>.

In-situ SEM investigation on the damage behavior of an interpenetrating metal ceramic composite

Philipp Christopher Morbitzer, Joél Schukraft^{*}, Christoph Lohr, Kay André Weidenmann

Institute of Materials Resource Management, Augsburg University, Am Technologiezentrum 8, 86159 Augsburg, Germany

1. Introduction

Protecting the environment and using resources economically has become increasingly important in recent years. The development and research of lightweight materials are of great importance in the mobility and transport sector [1]. In particular, the focus is on saving energy and reducing CO₂ emissions. The development of metal-matrix composites (MMCs) offers the potential to improve the properties of lightweight metals, such as aluminum. The advantages of metal and ceramic are combined in the composite materials and negative properties are to be kept to a minimum. The improved properties should reduce the amount of material used and, as a result, save weight and optimize energy consumption [2].

Interpenetrating phase composites (IPC) have a more complex 3D structure compared to particle or fiber composites due to the two continuous components [3,4]. The interpenetrating metal ceramic composite (IMCC) investigated in this work consists of a highly homogeneous and fine porous alumina foam and the AlSi10Mg aluminum cast alloy. The low-cost ceramic preform was manufactured by Morgan Advanced Materials Haldenwanger GmbH, which holds a patent on this manufacturing process [5].

This work contributes to the study of the innovative material in terms of its mechanical properties and microstructure with respect to mechanical loading. The material has already been investigated for

compression failure behavior using in-situ computed X-ray tomography experiment [6]. Based on this, more detailed microstructural investigations will be carried out and the fracture behavior will be examined. In-situ scanning electron microscopy (SEM) experiments are better suited for the analysis and recording of the microstructure. Due to a higher resolution and better phase contrast, additional influences like precipitates can be observed. In addition of the energy dispersive X-ray spectroscopy (EDX) measurements, this work contributes to the preliminary investigation of the fracture behavior of the IMCC. A decisive disadvantage of in-situ SEM investigation is that no influence of the 3D structure can be considered. Compared to post-mortem or ex-situ investigations, in-situ experimental setups have the advantage that the sample must not be mechanically unloaded for the investigation. Cracks are held open during the investigation, as the applied load is held. Therefore, higher crack visibility is guaranteed, and each phase of the experiment can be recorded without additional effort.

The objective of this study is to gain a better understanding of the properties of interpenetrating materials, with respect to their microstructure and associated damage mechanisms. Specifically, an aluminum-alumina composite material manufactured by gas pressure infiltration and consisting of a highly homogeneous and fine-pored Al₂O₃ microstructure and an AlSi10Mg cast alloy is investigated. During in-situ experiments under a SEM, tensile and compressive properties of the specimens are recorded and analysed by DIC. Due to the

^{*} Corresponding author.

E-mail address: joel.schukraft@mrm.uni-augsburg.de (J. Schukraft).

microstructure of the composite, DIC can be applied directly to the SEM images without the need of a speckle pattern. The microstructure analysis and DIC results will be correlated with the stress levels to provide a detailed insight of the damage behavior in interpenetrating metal-ceramic composites.

1.1. Related compression damage investigations in literature

Essential parameters in the investigation of IPCs or MMCs consisting partly of a ceramic, are the ceramic content, the distribution of metallic phase and ceramic and the fabrication method of preform and composite [7]. For example, composites with a considerable degree of closed porosity typically have a lower compression strength [8]. A finer microstructure, on the other hand, tends to result in higher compression strength, as there is a lower probability of critical defects [9–11].

Only few publications on IMCCs deal with crack initiation, crack growth and fracture behavior in a precise way as in this paper. However, the material behavior and the evaluation methods differ significantly between the different publications. Therefore, a direct comparison should be made with caution. In the following, investigations on the damage behavior of IPCs and MMCs are presented.

1.2. Compressive behavior

Roy et al. [12] analysed the internal load transfer and damage propagation under tensile and compression conditions. The lamellar interpenetrating phase composite was made of an Al_2O_3 preform and an AlSi12 cast alloy. The ceramic was manufactured using a pore-forming agent and a pyrolysis process. The experiments revealed that the load is transferred from the aluminum matrix to the stiffer and harder alumina matrix. In ceramic-rich regions, the constriction of the alloy by the ceramic leads to a suppression of plastic deformation. This increases the stresses and the formation of cracks. Further studies on the in-situ investigation of the internal load transfer of the lamellar metal-ceramic composite can be found in Roy et al. [9,13]. By in-situ SEM imaging, it was discovered that the failure of the composite results from the propagation of cracks in the ceramic-rich regions at 45° to the loading direction. Damage occurred first in the ceramic, which spread to the metallic phase at higher loading stages. Local debonding at the interphase was observed as well.

Scherm et al. [1] performed tensile and compression tests on an interpenetrated AlSi9Cu3/ Al_2O_3 composite. The preform was fabricated by cold pressing fine grained ceramic alumina powders containing pyrolysable pore formers followed by burnout and partial sintering and was infiltrated by die casting. The MMC had a metal content of 52–55 %. With a ceramic content of almost 50 %, the material did not show any macroscopic plastic deformation. The material sheared at an angle of 45° to the direction of loading. Post-mortem SEM images indicated the plastic deformation of the metallic phase and the chipping of the ceramic phase.

F.-C. Wang et al. [14] studied the damage propagation under dynamic load in a SiC/Al IPC. The uniaxial dynamic compression experiment was performed using a Split Hopkinson Pressure Bar. The composite was manufactured by vacuum pressure infiltration and the cells of the preform measured an average radius of 20 μm . The structure of the SiC preform was reconstructed by micro computed tomography. The damage was determined to be caused by the shear stress and is localized along the direction of maximum shear stress. The same composite was investigated by Li et al. [15] under similar conditions. In addition to the existing 3D simulation, an interface model was added. The results indicated that the cracks mainly originate in the SiC at the SiC/Al interface. The cracks propagate from the interface into the ceramic phase in the direction of compression. Through interface softening mechanisms, the cracks were deflected before forming the main crack.

1.3. Tensile behavior

Kaveendran et al. [16] analysed a hybrid ($\text{Al}_3\text{Zr} + \text{Al}_2\text{O}_{3\text{np}}$)/2024Al metal matrix composite. The composite is manufactured by reaction hot pressing and shows a significant reinforcement to the 2024Al matrix. Different sintering processes are applied to compare the microstructure and mechanical properties. The as-sintered status corresponds to a treatment at 600°C for 1 h under a pressure 25 MPa. The microstructure analysis reveals that a continuous Zr_2O layer has formed around the α -aluminum. Therefore, the α -phase is not interpenetrating, which is reflected in a lower tensile strength compared to the longer sintered sample and can be seen on the fracture surface. Sintering at 840°C shows a network structure of Al_3Zr particles and Al_2O_3 nanoparticles and strengthens the material. The crack in the longer sintered composite propagates along the $\text{Al}_3\text{Zr} + \text{Al}_2\text{O}_3$ phase and does not penetrate the large matrix regions and therefore dominating the composite performance. Al_3Zr particles exhibited brittle cleavage fracture properties, indicating strong interfacial bonding between the aluminum matrix and Al_3Zr reinforcements. Moreover, cracks in the Al_3Zr reinforcements show that it contributes to the reinforcement and load bearing capacity of the composite. The 2024Al phase contributes to the ductility of the composite, which is illustrated by dimples in the fracture surface images.

An interpenetrating $\text{Al}_2\text{O}_3/\text{Al}(\text{Si})$ composite, also known as C^4 composite, was investigated by Vecchina et al. [17] for its mechanical properties and was related to the composite microstructure. The C^4 composite was manufactured by reactive metal penetration using pure aluminum and an AlSi alloy and consists of 63 % ceramic and 37 % metal. The microstructure displayed an interpenetrating structure. Only at the sample surface the phases are distributed homogenous and form the surface to the center the aluminum developed columnar like structure. The fractography of the mechanical tests revealed the splitting of the brittle ceramic and the dimples of the ductile metal. The plastic deformation of the metallic phase indicated that the ceramic contributes to the stiffness and resistance of the composite. At the same time, the aluminum supports the composite after failure.

In addition to the compression tests, Scherm et al. [1] carried out tensile experiments on the composite described before. For small strains, the material exhibited a linear behavior, which changed to a non-linear behavior at higher loads. This can be explained by the plastic deformation of the metal at higher stresses. The normal stress led to the failure of the material, which is characterized by the fracture plane perpendicular to the applied load. Due to the ductile deformation of the metallic phase, dimples can be seen on the fracture surface of the metal phase. The failure of the ceramic preform is observable by a brittle crack surface and are mainly parallel to the fracture plane.

Srivatsan et al. [18] analysed tensile experiments on an AA2009 aluminum alloy reinforced by silicon carbide particle and investigated the fracture surface. The composite was produced by a powder metallurgy process. Low ductility was observed macroscopically; in contrast, ductile and brittle mechanisms were observed locally at the microscopic level. The crack grew along the matrix between the reinforcing particles. Also, failure of the particles and debonding at the phase boundaries allowed the microscopic cracks to grow, resulting in macroscopic failure.

Zhou et al. [19] studied the fracture behavior of an $\text{Al}_2\text{O}_3\text{-TiC/Al}$ IMCC using in-situ SEM investigation. The preform was infiltrated via gas pressure with pure aluminum and 2024Al alloy. The material showed brittle failure perpendicular to the load direction. The fracture surface displayed both splitting of the ceramic reinforcement and deformation of the matrix. Cracking in the reinforcement was found to be the predominant mode of failure. The ceramic could fail due to its relatively low strength or due to overstressing under tension. The fracture was bridged by plastic deformation through the Al-matrix, thereby significantly increasing the toughness of the composite.

2. Materials and methods

2.1. Materials and composite manufacturing

The IMCC is based on a highly homogeneous and porous Al₂O₃ ceramic foam. Open-cell ceramic foams can be produced by a slurry-based processing route. For the investigated IMCC, the alumina preform was provided by Morgan Advanced Materials Haldenwanger GmbH (Waldkraiburg, Germany). The ceramic foam was already examined by Horny et al. together with the authors [20] with regards to porosity and pore size. Using analysis-ray computed tomography, a porosity of around 74 % and an average pore radius of 14.39 μm were determined and shown results in good agreement with further methods, as mercury porosimetry, helium gas pycnometer method and Archimedes principle.

The investigated IMCC was manufactured via gas-pressure infiltration with an AlSi10Mg cast alloy. The components were heated to 700 °C in a vacuum sealed furnace with a residual pressure of $2 \cdot 10^{-2}$ mbar. After melting of the cast alloy, an argon gas pressure of 60 bar was applied on the melt. After 10 min dwell time, the chamber is cooled down to room temperature maintaining the gas pressure and the solidified composite can be removed for sample preparation. A detailed description with a schematic drawing of the process layout can be found in Horny et al. [20].

For comparison of the tensile experiment, on the one hand the AlSi10Mg as received, hereafter referred to as AR, and on the other hand the excess aluminum out of the infiltration process, hereafter referred to as IF, were prepared as described below.

2.2. Sample preparation

Squared samples were prepared for the in-situ compression investigation. A diamond wire-saw by Diamond Wiretec was used for sizing of the composite into cuboids with an edge length of 4 mm. To achieve plane parallel surfaces the samples were grinded with abrasive SiC grinding paper of P800 with the Struers Tegramin 25 grinding machine. The final dimensions of the 10 tested samples were measured using a Tesa μ-Hite vertical length gauge. The cuboids had a edge length of approx. 3.4 mm. The specimens were polished following the recipe presented in Wegscheider et al. [21] and is listed in Table 1.

For the tensile experiments four samples of the IMCC and four samples of the aluminum alloy were used and pre-cut with the diamond wire-saw into $40 \times 4.25 \times 8 \text{ mm}^3$ bars. The ultrasonic 40 universal machine from DMG MORI equipped with diamond grinding pins was used for milling the specimens. The final geometry was a notched bar as it can be seen in Fig. 2. For the calculation of stress and strain, the dimensions of the notch were taken. Accordingly, the length of the indentation was determined as the original length of the specimen, which corresponds to 11 mm for all specimens. The cross section is composed of the width of the notch of 3.5 mm and the thickness of approx. 3.5 mm. For the further surface preparation the same steps as for the compression samples were performed.

Table 1
Polishing steps to prepare the composite specimens for microscopy.

Polishing cloth/film	Suspension	Contact pressure	Circulation	Duration
MD Largo	Diamond suspension, 9 μm	25 N	Synchronous 210/150 rpm	8 min
MD DAC	Diamond suspension, 3 μm	25 N	Synchronous 210/150 rpm	5 min
MD DUR	Diamond suspension, 1 μm	20 N	Synchronous 210/150 rpm	5 min
MD CHEM	OP-S suspension with rinse agent	15 N	Synchronous 210/150 rpm	2:30 min

2.3. Microstructure analysis and in-situ testing

The microstructure of the composite was investigated using the ESEM mode of the Prisma E SEM from ThermoScientific. For the investigated material system, different advantages of the ESEM mode surpass the high vacuum mode with sputtered samples. For the ceramic preform with its rough and porous surface, sputtering only works partially. For the investigations on the IMCC, an artifact free surface plays a key role for the clear assignment of occurring damage. Sputtering of thick layers can cause cracks in the sputtered layer and influence the examination. For EDX mapping, the sputtered element creates an additional peak, influencing the composition of the material constitution and creates additional uncertainties, by shielding the reflecting material specific radiation. Therefore, coating of an electrically conductive, sputtered layer was not used. The beam parameters such as working distance, magnification and spot size are given in each image individually. The EDX mapping recordings were acquired over a period of 180 s at a voltage of 20 kV and an electric current of 1nA. At the selected 10 mm working distance a dead time of 3–4 % was registered and about 20,000 counts per second were detected. The point analyses were performed with the same beam parameters and counts per second and were recorded over a period of 60 s.

For the in-situ experiments, a Tensile/Compression module from Kammrath & Weiss GmbH (Schwerte, Germany) was used. The module was equipped with a 10 kN load cell and a linear glass scale is attached to the module to record the displacement. This sensor measures the movement of the holders and has a resolution of 0.1 μm. The compression experiments were carried out at a speed of 0.5 μm/s and the tensile testing was performed at a speed of 0.25 μm/s. Compression stamps for the module were designed and manufactured internally (see Fig. 2). The in-situ tensile set-up and the specimen geometry is shown in Fig. 1.

The recordings of SEM images for the 2D digital image correlation (DIC) investigation were captured with a rate of 1 Hz by the software of the Module and can be directly assigned to the stress–strain diagram. The program ARAMIS Professional from GOM Correlate was used for the evaluation. For this purpose, the SEM image series was imported, and the natural microstructure of the composite used as a recognizable pattern on the sample surface. The first image in the preloaded state was selected as a reference. The strain over a defined area is calculated and the program identifies the different strain levels in a color spectrum. During the in-situ experiments the working distance needed to be increased up to a minimum of 17.3 mm, so that the stage fits below the beam source. It was not possible to utilize the ESEM mode since the sample was too far away from the detector and the signal became too weak. Therefore, the high vacuum mode was used during the experiment with unsputtered samples, as explained above. Local charching effects were prevented as far as possible with the chosen parameter. The SEM images were taken in the line scanning mode and with a speed of 45 μs. The image resolution was chosen to 768×512 pixels with a pixel length of ca. 8 μm. The facet size was chosen to 19 pixel with a distance of 16 pixel, so the strain resolution is about 0,0012 mm². The other parameters are given in the corresponding figures. In this paper, representative measurements are shown and analysed.

3. Results

3.1. Microstructure analysis

The following chapter focuses on the microstructure of the composite and its components, the determining factor for the investigation of the fracture mechanisms and the damage. For this purpose, ESEM images were used and EDX recordings were included to determine the composition of the different phases.

The images of the foam structure in Fig. 3 give insights into the pore morphology. Both the interconnection between the pores and the ceramic struts are shown. At higher magnification, the grains and their

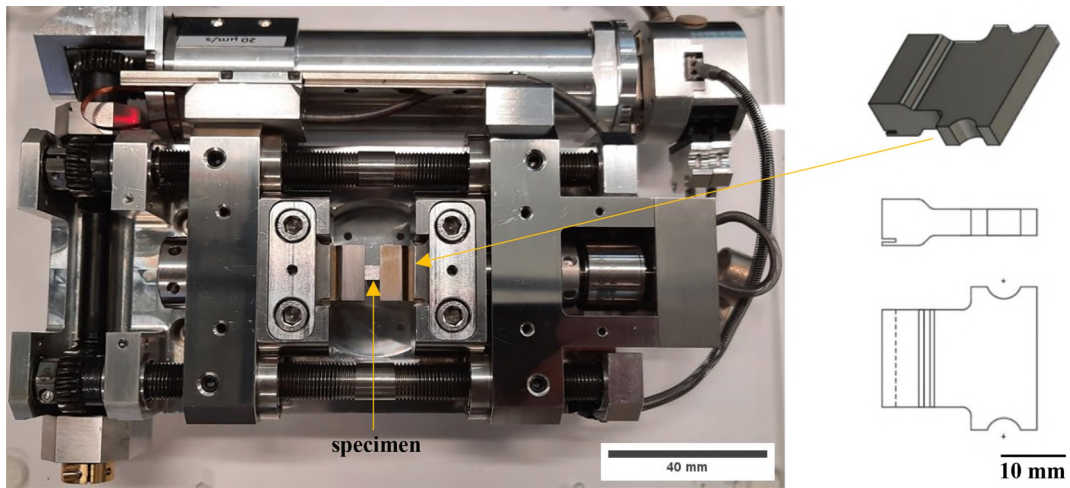


Fig. 1. In-situ compression setup with a specimen (ca. $3.4 \times 3.4 \times 3.4 \text{ mm}^3$) mounted between the designed compression stamps (details on the right).

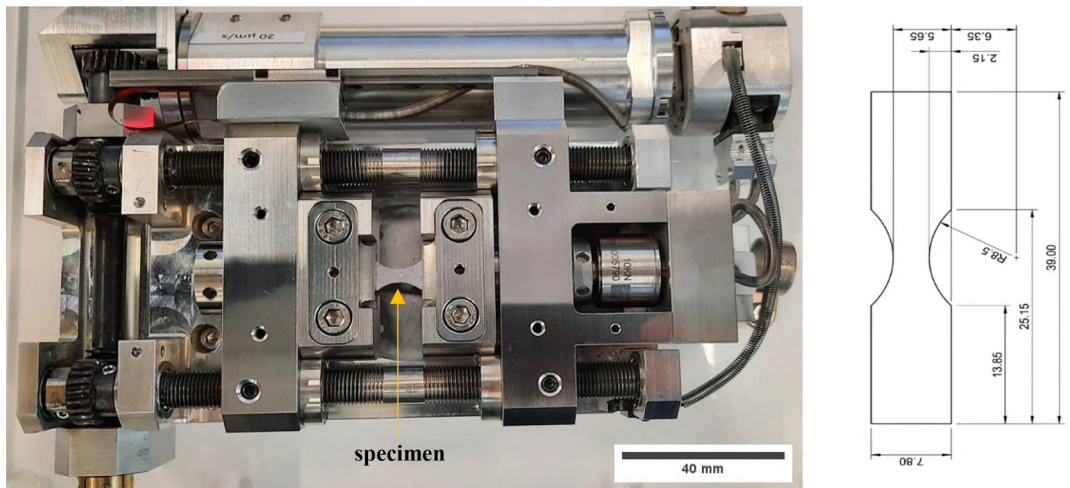


Fig. 2. In-situ tensile setup with mounted specimen and its geometry (details on the right with length specifications in mm).

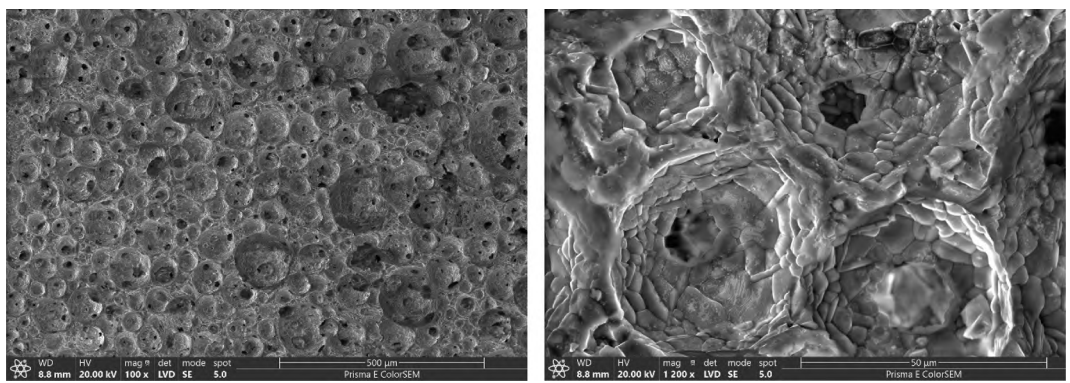


Fig. 3. ESEM recording of the foam microstructure at 100x (left) and 1200x magnification (right).

boundaries can be distinguished. Sintering in the manufacturing process can create three types of inaccessible porosity within the foam: Closed pores can result from missing connection to neighboring pores. In addition, in nano- and low micrometer range, intragranular and intergranular pores can be formed. Intergranular pores are in the areas of converging grains and are identified by their angular shape. Intragranular pores are formed inside the grains and are roundish.

In the Fig. 4 a comparison between the microstructure of the two aluminum samples is presented. The as-received (AR) alloy is shown at a magnification of 2500x on the left and the alloy's microstructure after infiltration (IF) at a magnification of 650x on the right. In the Table 2 (AR) and Table 3 (IF) the results of the point EDX measurements are listed. The microstructure of the AR aluminum displays large and elongated areas, which are separated by lighter precipitates on the one

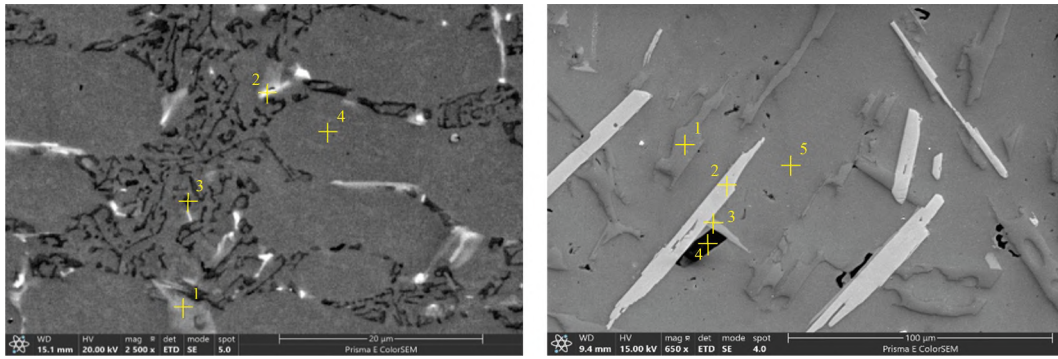


Fig. 4. SEM images of the aluminum microstructure in the as-received (left) and the infiltration (right) state with the marked spots of the EDX point measurements.

Table 2

Results of the EDX measurement of the mapping measurement and the point analyses corresponding to the locations from the AR alloy in the left image in Fig. 4 in weight percent for the AR aluminum.

Element	Overview (Mapping)	Point 1	Point 2	Point 3	α -Aluminum Point 4
Mg	0.4	4.1	5.9	0.3	0.0
Al	86.0	75.6	71.8	65.2	97.6
Si	12.9	15.8	15.7	34.1	2.3
Mn	0.3	1.0	1.7	0.2	0.1
Fe	0.4	3.5	5.0	0.1	0.0

Table 3

Results of the EDX measurement of the mapping measurement and the point analyses corresponding to the locations from the IR alloy in the right image in Fig. 4 in weight percent for the IF aluminum.

Element	Overview (Mapping)	Point 1	Point 2	Point 3	Point 4	α -Aluminum Point 5
O	0.8	0.4	1.2	1.0	29.7	0.8
Mg	0.2	0.1	0.0	16.6	0.0	0.2
Al	75.3	1.5	53.4	46.8	49.2	97.4
Si	21.7	97.6	17.8	26.4	21.0	1.6
Mn	0.4	0.0	5.0	1.7	0.0	0.0
Fe	1.6	0.1	22.6	7.5	0.0	0.0

hand and surrounded by fine distributed darker, needle-like precipitates on the other hand. Point 1 and Point 2 reflect the precipitates and are illustrated brighter in the recordings. These usually accumulate near or between two α -aluminum regions. They possess a certain amount of magnesium-, manganese- and iron-rich precipitates (see Table 2). The Point 3 samples a primary silicon precipitate, which is finely dispersed throughout the sample. The large area phases were analysed in Point 4 and reflect the α -aluminum phase. The microstructure of the IF aluminum indicates four different precipitates. In the overview (Point 1) and the α -aluminum (Point 5) are visible (see Table 3). Point 2 samples an iron and manganese rich precipitate, which still contains a clear ratio of silicon and aluminum. These precipitates also emerge in the form of needles. A magnesium-rich precipitate was found at Point 3. These occur only in small amounts in the alloy and are mostly in a branched form. A particularly high oxygen content was observed at Point 4 in the dark precipitates, which are bulky and very rarely present. As an aid to the more detailed analysis of precipitations in

Table 4

Measured values in wt. % of spark spectroscopy of the aluminum alloy under study. \bar{M} stands for the mean value, S for the standard deviation.

	Si	Fe	Cu	Mn	Mg	Cr	Ni	Zn	Ti	Al
\bar{M}	10,256	0,465	0,042	0,183	0,237	0,007	0,004	0,002	0,052	88,728
S	0,348	0,141	0,012	0,014	0,094	0,002	0,002	0,002	0,004	0,432

the metallic phase, the spark spectroscopy of the cast alloy was performed and the measured element ratios are given in the Table 4.

The ESEM image of the IMCC in Fig. 5 shows a clear contrast between the lighter ceramic and the darker metal phase. The preform displays no microstructural changes or damage after gas pressure infiltration. Non-infiltrated sectors are indicated by black areas. These can be tracked back to two main locations. On the one hand, there is some minor closed porosity in the preform, indicated by small spherical areas. On the other hand, non-infiltrated areas at the ceramic-metal interface or at the interface of two filled cells can be seen. Fig. 6 displays the area of the EDX measurements. The area was analysed by an overview mapping and the enrichments were investigated by point measurements. Table 5 contains a list of the element contents in weight percent. The element-specific mapping images provide information about the position and composition of the precipitates.

In the ESEM mode the precipitates are also distinguishable in shape and contrast. Point 1 samples an area with primary silicon. These zones differ only slightly from the aluminium phase in the ESEM mode and localize mostly at the interface of the metallic phase. Point 2 is located within an easily recognisable precipitate that shows no discernible dependence of positioning in the metallic phase. It is primarily

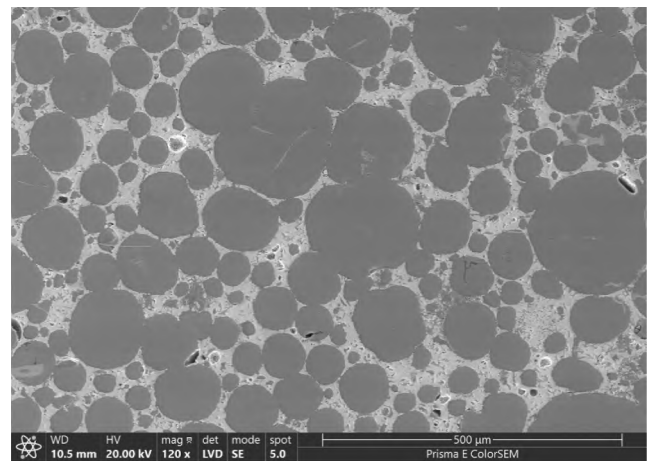


Fig. 5. ESEM image of the polished IMCC. The lighter area represents the ceramic phase and the darker the metallic phase. Non infiltrated areas are indicated in black.

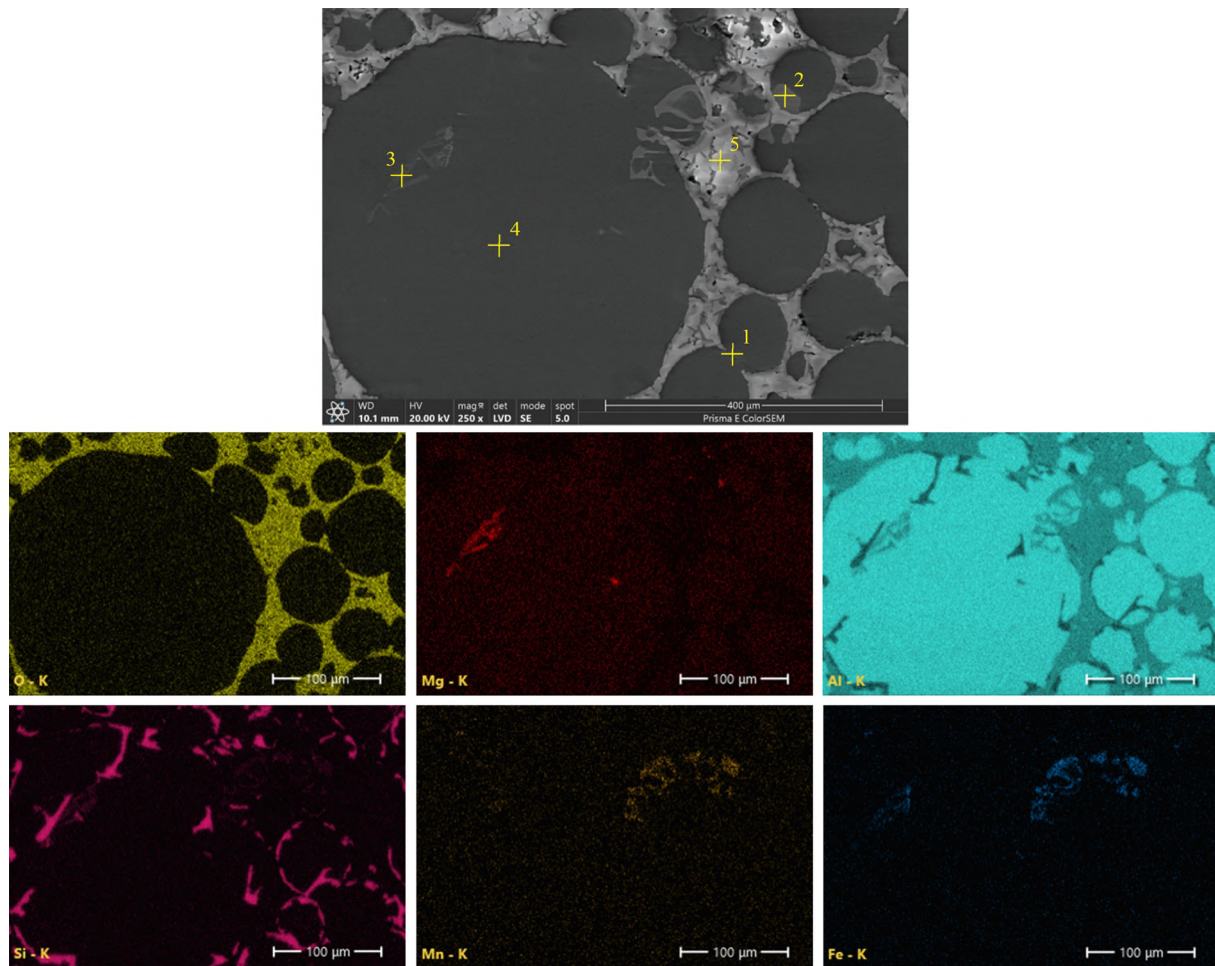


Fig. 6. ESEM image of the EDX mapping area of the IMCC (top). The mapping of the single elements in color are matching the ESEM image. From top left to bottom right: Oxygen (yellow), Magnesium (red), Aluminum (turquoise), Silicon (pink), Manganese (orange), Iron (dark blue). The points marked in the overview photo are the locations of the EDX point analyses listed in Table 5. (For interpretation of the references to color in this figure legend, the reader is referred to the web version of this article.)

Table 5

Results of the EDX measurement of the mapping measurement and the point analyses corresponding to the locations from Fig. 6.

Element	Overview (Mapping)	Point 1	Point 2	Point 3	α -Aluminum Point 4	Preform Point 5
O	16.3	4.7	4.1	3.3	5.7	40.7
Mg	0.2	0.1	0.1	6.6	0.3	0.0
Al	63.3	21.5	62.5	64.9	89.8	56.5
Si	11.5	73.6	9.4	20.2	4.1	2.6
Mn	0.0	0.0	8.8	0.5	0.1	0.1
Fe	0.1	0.1	15.2	4.5	0.0	0.2

composed of aluminium and iron, but also includes a certain amount of manganese and silicon. Magnesium was only detected in Point 3 in a striking amount. In addition, the precipitate also contains aluminium, silicon and iron. These precipitates are found in small quantities within the metallic phase and are characterised by their branched form. For comparison, spot EDX measurements were taken both from the metallic phase without visible precipitates, the α -aluminum phase (Point 4), and from the preform (Point 5). When examining the precipitation, it was noticed that even before the experiments, visible defects could locally be found at the interfaces of the different phases of the alloy.

3.2. In-situ compression experiments

In this chapter, the curve of a representative stress–strain diagram is

described and the data of the DIC evaluation is presented. In addition, the damage of the microstructure at different load levels is illustrated.

The stress–strain diagram is plotted in Fig. 7. For the measurement of the displacement, the data of the linear glass scale of the module are taken. During the experiment, high resolution SEM images of the microstructure were recorded and therefore the experiment was paused. This is reflected in the data by a dip of the stress. The composite shows a maximal compressive strength of 325 MPa. A linear increase is observed at first, which flattens out before reaching the maximum. After, the graph drops by 40 MPa. The investigated composite shows a constant residual resistance of 280 MPa. This plateau also shows no changes up to an elongation of 290 μ m, which equals to 9 % compression strain, where the test was stopped.

For the DIC evaluations, the images were imported into the GOM

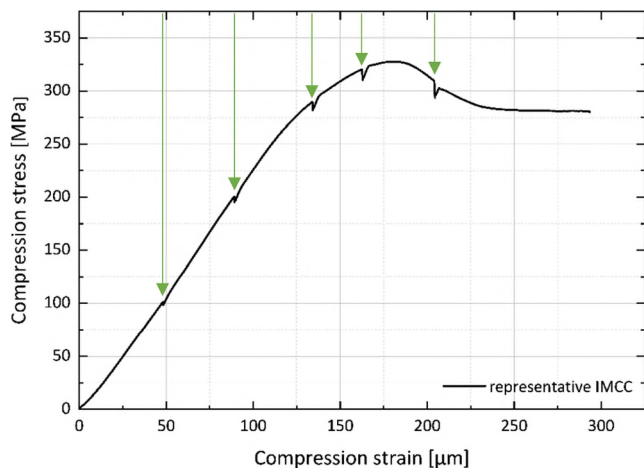


Fig. 7. Representative stress–strain diagram with arrows marking the dip of the stress through pausing the experiment.

Correlate programme (see Fig. 8). A homogeneous increase in strain can be observed within the elastic range. With increasing stress, the strain increases at weak points along 45° to the direction of the force. The weaker areas of the specimen can already be highlighted before damage sets in. In the further progress of the experiment, cracks and clear failure of the composite occur first at these spots. Along the main crack in 45° direction, the sample experiences a shear crack and slides off.

The microstructure was recorded at selected locations at load levels of 100 MPa, 200 MPa, 290 MPa, 320 MPa, 310 MPa and before and after the test using SEM. The sequence of images is displayed in Fig. 9. The first change can already be observed at 100 MPa in the elastic range of the stress–strain diagram. Defects localised along precipitates show a propagation. At a stress of 200 MPa, new damage is visible. First micrometre-sized cracks propagate in the ceramic and local debonding along the phase boundary is indicated. No formation of cracks was visible in the images used for the DIC investigation. However, the DIC

indicates that stress fields have already been built up in the composite. In addition, the plastic deformation of the metallic phase causes cracks along the precipitates. Before the stress maximum, the damage described above continues to progress and cracks in the ceramics continue to develop. After the failure, the deformation is so significant that metal-filled pores are sheared off and cracked.

After the experiment the fractured composite was investigated again in the ESEM mode. Fig. 10 presents an ESEM image of a deformed interface between two pores. This area is located along the main crack in the middle of the sample. The EDX mapping illustrates that cracks are exclusively located in or along the precipitates. Plastic deformation is presented in the precipitation-free areas only.

3.3. In-situ tensile experiments

The representative curves of the IMCC and the aluminum specimens are presented and compared in this chapter. Images and EDX recordings of the fractured specimen surface and the crack surface of the IMCC should provide a detailed insight into the fracture behavior.

The DIC evaluation for the tensile experiments of the polished specimens exhibit disturbing interferences due to the low contrast in the metallic phase. Alternative unpolished, plane-parallel specimens were examined. The signal improved, but due to the low elongation, no interpretable stress field was observed. Also, SEM images were acquired during the experiment. However, the analysis of the in-situ tensile experiments is more difficult to realize. The specimen is loaded during the image recording, in order not to close the damage that has developed. While taking the recordings at higher load levels, it occurred that the specimen broke despite pausing the test.

The stress–strain curves of the IMCC and the AlSi10Mg alloy can be seen in Fig. 11. As in the compression experiments, the calculation of the tensile stress and strain are based on the data from the module. For the calculation of stress and strain, the dimensions of the notch were taken (cf. 2.2).

The IMCC tends to a brittle behavior and achieves an elongation at fracture of around 109 μm or 1 % and a maximal tensile strength of

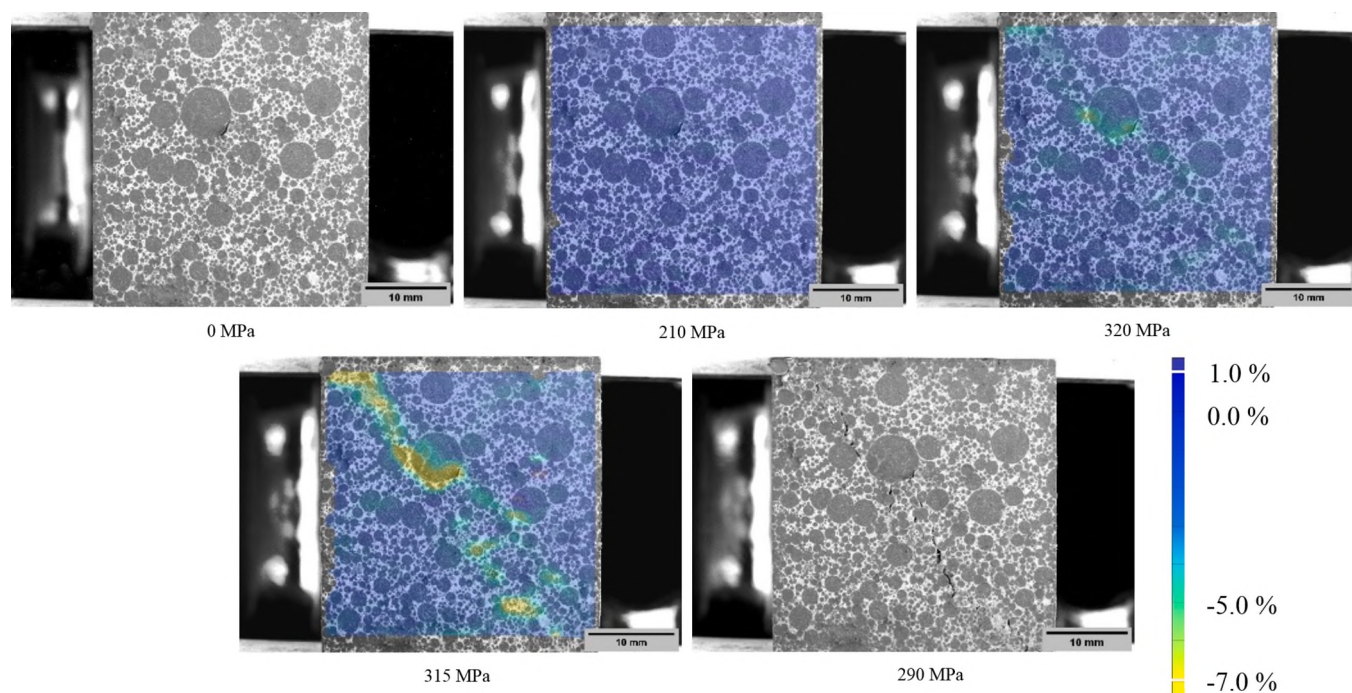


Fig. 8. SEM recording of the micro cracking in the microstructure. The orange arrows indicate the propagation of the defects located at the precipitate interface. The yellow arrows indicate microcracks of the ceramic and the local debonding. (For interpretation of the references to color in this figure legend, the reader is referred to the web version of this article.)

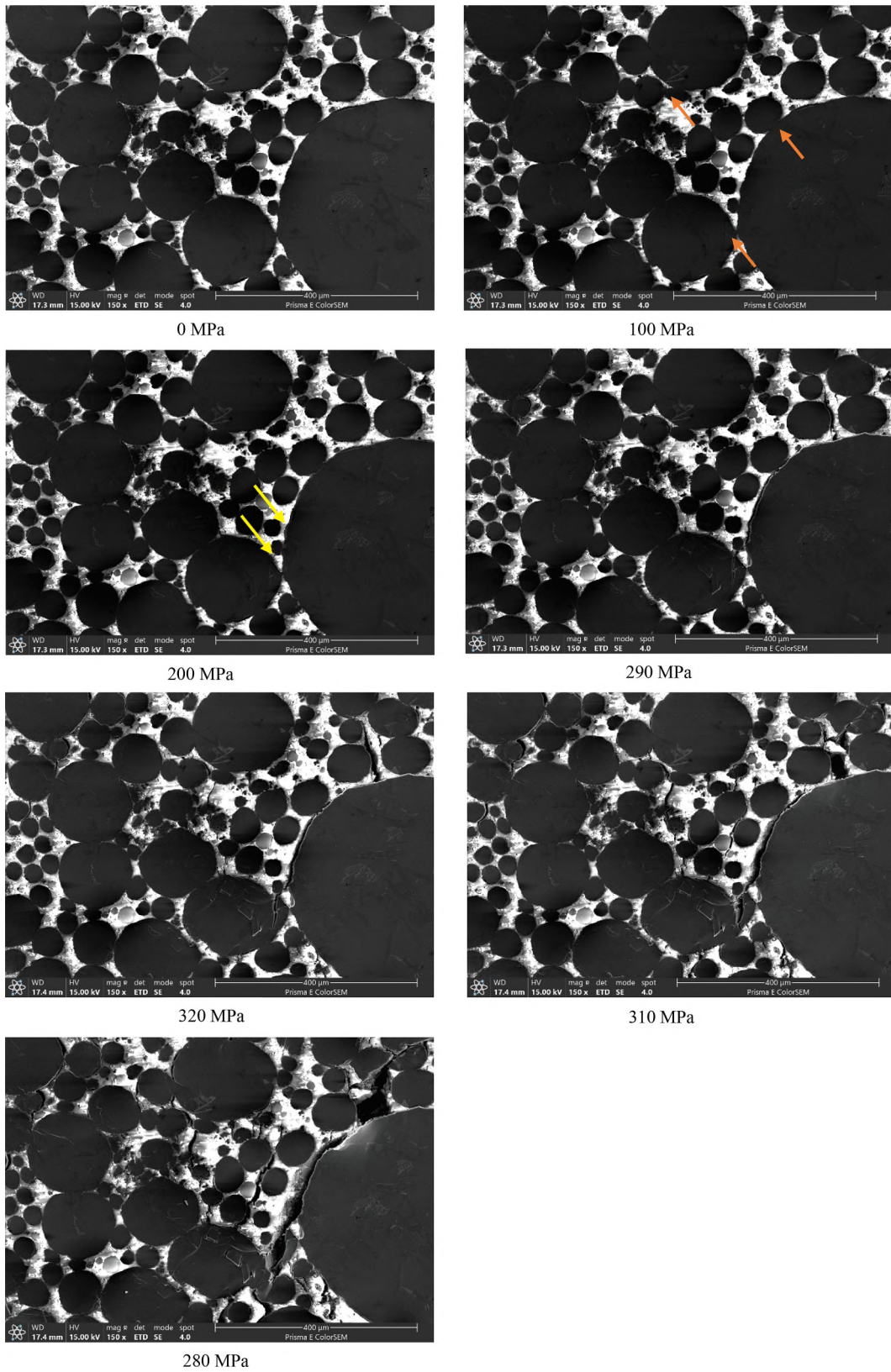


Fig. 9. SEM recording of the micro cracking in the microstructure. The orange arrows indicate the propagation of the defects located at the precipitate interface. The yellow arrows indicate microcracks of the ceramic and the local debonding. (For interpretation of the references to color in this figure legend, the reader is referred to the web version of this article.)

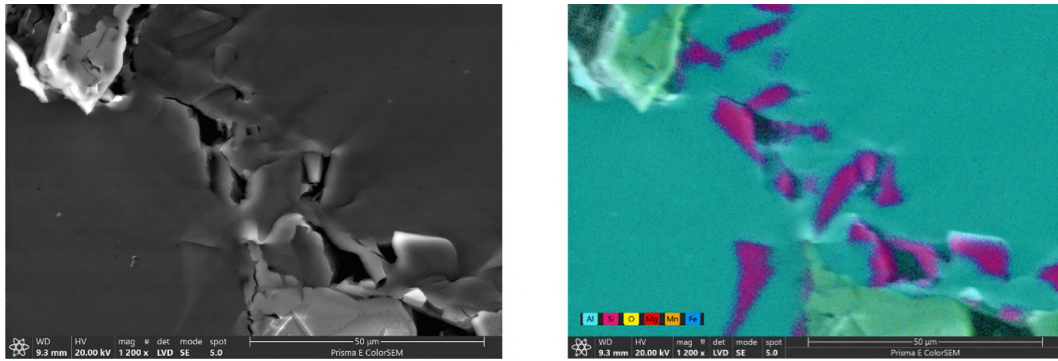


Fig. 10. ESEM image (left) of a deformed interface between two filled cells and the associated EDX mapping image (right).

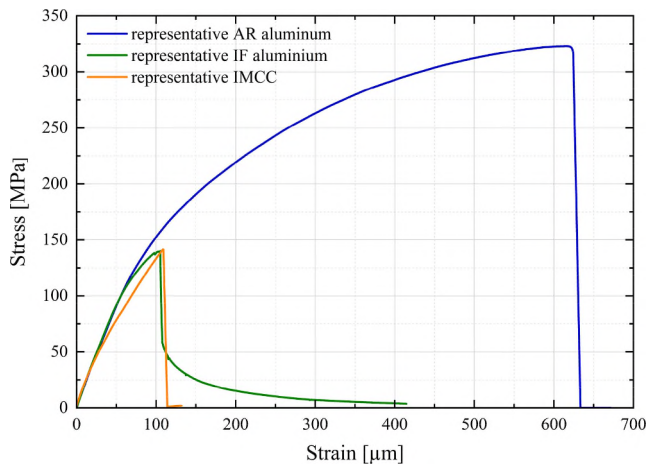


Fig. 11. Representative stress-strain diagrams of the tensile experiments on IMCC (orange) and AlSi10Mg alloy in the as-received (blue) and the infiltration state (green). (For interpretation of the references to color in this figure legend, the reader is referred to the web version of this article.)

141.5 MPa. The aluminum specimens show a higher toughness and a ductile behavior. The AR aluminum deformed plastically up to 620 μm, which equals to 5.7 %, and reached a tensile strength of 323 MPa. The IF aluminum already experienced a drop at 139.9 MPa. The plastic deformation with a flattening of the curve becomes visible before the maximum is reached (also in comparison to the IMCC sample). However, the specimen did not fail completely at 105 μm or 0.95 % elongation, but dropped to 59 MPa. As the strain increases, the stress slowly decreases until it reaches zero.

During the examination of the fractured sample surface, three main crack locations were identified. Representative images are shown in Fig. 12. In all images, fracturing of the ceramic phase and the debonding of the interface between the ceramic and the alloy can be seen. Crack branching and plastic deformation of the metallic phase can be observed on the recording in the top left. The top right reveals breakage of the specimen along the brittle precipitates. In the lower image, both the failure along the precipitate and a clear plastic deformation of the metallic phase is visible. In the corresponding EDX image, the fracture occurs preferentially along the precipitates, but the crack is also bridged by plastic deformation.

A further investigation of the fracture behavior is provided by the analysis of the crack surface. Representative recording with the corresponding EDX mapping is given in Fig. 13. The pictures illustrate that many of the filled pores have broken out of the ceramic. Brittle fracturing of the preform can also be noted. The matching EDX image shows the area of precipitates on the fracture surface. A clear example is given in the middle image. Here, a smooth fracture can be seen along an iron-

containing precipitate. In comparison, a detached pore can be seen in the bottom image. Dimples can be seen in the α-aluminum phase.

4. Discussion

An important point in the discussion is, that this work can only provide a two-dimensional insight. No statement, except on the crack surface of the tensile experiments, can be made about the damage behaviour in three-dimensional space. A 3D-analysis of the damage behavior of the investigated IMCC has already been performed and published by the authors [6,22] and will be taken into consideration in the following.

4.1. Microstructure analysis

SEM examinations of the IMCC revealed relevant aspects of the microstructure, which could be determining factors for the fracture mechanisms and the damage. The investigated AlSi10Mg/Al₂O₃ has a residual porosity of 3 %, as shown by the measurements of Horny et al. [20]. The CT-measurements were compared to other methods, as the helium gas pycnometer and Archimedes principle and the reliability of detection is described elsewhere (compare [23]). The non-infiltrated areas, indicated by their black appearance, can be distinguished in two types. The closed porosity, displayed by small spherical areas, are caused by the slurry-based manufacturing route of the preform, as described above. The second type are the casting defects caused by the gas pressure infiltration. The fabrication of composites with interpenetrating phases is a complex process that can lead to process-induced defects caused by various factors. Basista et al. [24] summarized these difficulties for the fabrication of alumina/aluminum IPCs. The fabrication of ceramic preforms with open porosity above the percolation threshold and sufficient mechanical strength is a thorny issue. Additionally, the fabrication of infiltrated aluminum/alumina composites with graded porosity complicates the process due to the complexity of the structure and poor wettability by molten aluminum.

Not completely filled pores and local debonding between the two cells might be caused by the solidification of the alloy. The metal contracts in the cooling process and stress fields develop, both in the metal phase and at the phase boundary. This thesis is supported by the investigation in Roy et al. [9]. Especially in the interface between two pores, this can lead to defects. Due to the high tortuosity of the ceramic foam, the infiltration paths for the metallic melt and small passages have to be passed in the connection between two pores. Therefore, it can happen that at the interfaces of two pores, the melt meets from two sides and does not bond completely. This phenomenon can also be observed in injection molding processes. Here, two mass flows meet and form a so-called flow line. Bociaga et al. [25] visualized the melt flow line in injection moulding.

By the EDX measurements, the metallic phase can be distinguished into α-aluminum and secondary phases (cf. Fig. 6 and Table 5). The

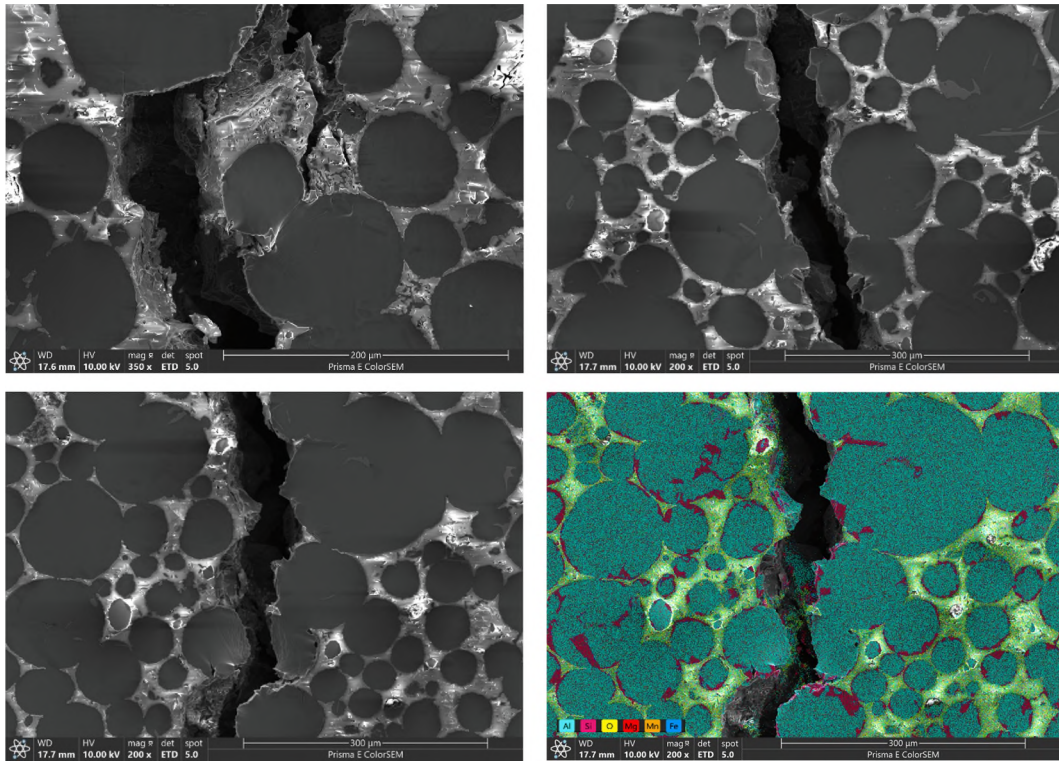


Fig. 12. Representative SEM images of the crack path through the materials phases and EDX analysis of the crack section from the bottom left image.

α -phase, as characterized in Point 4, consists mainly of aluminum. The secondary phases are the precipitates found in the metal throughout the composite. Fine dispersed precipitations lead to increased strength by impeding dislocation movement and dislocation pinning occurs at the interface. The contraction of the cast alloy during cooling can also lead to stresses on the formed precipitates. If the stress fields are too high even cracks on the brittle precipitates can occur [26,27]. These defects have an influence on the fracture behavior of the IMCC. Various publications have found that the hardness of AlSi10Mg is increased mainly by the brittle eutectic Si precipitates [28–30]. In cast alloy studies by Le Zhou et al. [31] and Aboulkhairet al. [32] it was observed, that eutectic silicon deposits mainly at the interphase. These findings are consistent with the results of the EDX investigations, evaluated here. If this brittle precipitate is located in the stress field of two adjacent cells, this can lead to local defects in the form of a crack. Point 2 and Point 3 of the EDX analysis consist of AlFeSiMn and α -AlFeSiMg (see Fig. 6) [28,33]. According to Voncina et al. [34], less Al_5FeSi precipitations are expected here, due to the high manganese content in the used AlSi10Mg alloy. However, the manganese content promotes the formation of $\text{Al}_{15}(\text{FeMn})_3\text{Si}_2$ precipitates. The high oxygen content in the metallic phase could be due to surface oxidation and/or the high oxidation tendency of aluminium [35].

The spark spectroscopy in Table 4 and the results of the EDX measurements in Table 5 coincide. Elements such as magnesium, manganese and iron are not detected in the EDX mapping, but accumulate selectively in the precipitates. Elements detected in the spark spectroscopy but not in the EDX can be counted as inaccuracies or irrelevant substances because of their low percentage of less than 0.1 %.

The aluminum specimens differ clearly from each other in terms of the microstructure. The AR material exhibits a fine dispersion of eutectic silicon, which surrounds the large-size α -aluminum regions. Due to the long cooling rate during the gas pressure infiltration, the precipitates were significantly enlarged. Dendritic precipitates are mainly seen in the IF samples, these were also observed by Takata et al. and Voncina et al. [34,36]. The IF microstructure matches with the already discussed

microstructure of the metallic phase of the composite. Neuser describes this microstructure as the typical silicon needle embedded microstructure in an α -aluminum matrix of an unmodified and slowly solidified cast aluminum alloy [37,38]. The data from the point EDX spectra are consistent with the precipitates already determined in the IMCC. Referring to Table 3, the presumption that the light grey silvery precipitates are composed of $\text{Al}_{15}(\text{MnFe})_3\text{Si}_2$ is strengthened [39]. The darker and more common needles are composed of primarily silicon and the smaller branched precipitates are made of α -AlFeSiMg.

4.2. In-situ compression experiments

The stress–strain curves of the IMCC under compression load are shown in Fig. 7. The preform has a linear increase of the stress–strain curve up to an ultimate compression strength of 60–65 MPa. The foam fails totally and the curve drops to 0 MPa [40]. The AR aluminum alloy shows a steadily increasing stress–strain curve, which goes beyond a compression of 10 % [40]. The composite has a linear increase at low loads, caused by the elastic deformation. The curve flattens out before the maximal strength as crack onsets are initiated at around 200 MPa. After the failure at 338 MPa, no sudden drop in stress is observed. Despite the 45° shear crack the composite was held together by the metallic phase. The stress level remains high as the introduced energy on the material is absorbed by the resistance of the metal and therefore can withstand further damage. The energy is absorbed by the hardening of the alloy and/or by interlocking of the fracture surface. The fracture at a 45° angle to the main loading direction was also observed in the publications with composite with high ceramic content [1,11,14,41].

The areas most affected by the damage are located along the $\pm 45^\circ$ orientation to the main loading direction, as it can be seen in the DIC illustrations in Fig. 8. This fracture behavior confirms previously published experiments on this IMCC in an universal testing machine and in-situ CT experiments [6,22]. At 210 MPa, the highest compression occurred measured 1.3 %, which increased to 3.5 % at 320 MPa. After the maximum compressive strength, this highest compression amounted

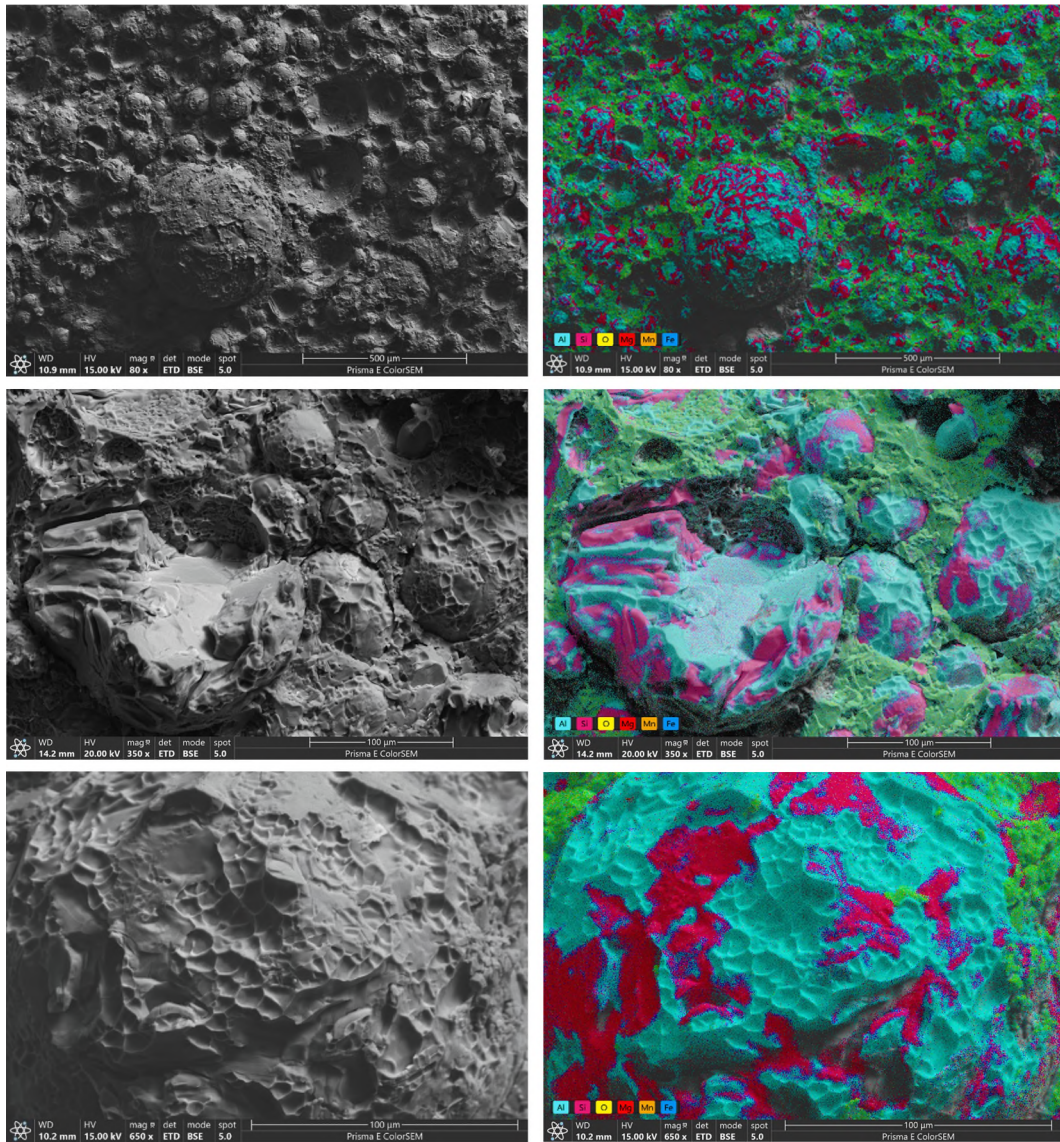


Fig. 13. Representative SEM images and corresponding EDX mappings of the crack surface of the IMCC.

6.9 % at 315 MPa.

Having a closer look at the microstructure during the experiment regarding the recordings in Fig. 9 different stages of damage propagation can be distinguished. The possible weak spots of the composite can influence the failure of the material, especially if they are at the diagonals. Weak points outside these zones experienced little or no damage and thus have no direct influence on the fracture behavior.

In Schukraft et al., the fracture behavior was divided into three mechanisms by CT evaluation [6,22]:

The damage initiation in the ceramics and interface, the increase in cracks and plastic deformation, and lastly the formation of the main shear plane. In this work a fourth mechanism was observed. The first signs of damage can already be observed at 100 MPa in the elastic range of the stress–strain curve. Before the crack initiation in the ceramic, defects localized along precipitates propagate around 25 μm in length due to the rising stress fields. Also, the elastic deformation of the α -aluminum phase contributes to increasing stress on the brittle precipitates, at a stress of 200 MPa new defects occur. Micrometer-sized cracks in the range of 30 μm propagate in the ceramic. Also, local debonding along the phase boundary is indicated. This supports the observed first stage of the CT investigations [22]. Also in other MMCs the same phenomena was monitored [12,41,42].

The plastic deformation of the metallic phase causes growing cracks along the precipitates. As the stress–strain curve flattens out, some of the energy is absorbed by the plastic deformation of the metallic phase. The damage described above continues to progress and fraction in the ceramics also continue to develop. The cracks in the ceramic are bridged over the metallic phase. This behavior reflects the second mechanism in the 3D-investigations of the IMCC [22]. These observations support the findings of the study by L. Wang et al. [41]. When the ultimate compression strength was reached, the material approaches the last stage of the damage behavior. The IMCC started to fail and the fracture propagated through the hole sample. As already described, the precipitates increase the strength of the metallic phase and prevent the early shearing of the metallic phases. At a nominal compression of 9 %, the deformation is so significant that metal is sheared off. The composite was not broken in two parts. The plastic deformation of the metal absorbed enough energy to give the specimen a residual resistance and prevent total failure. This is also explained by Bandyopadhyay et al. [43]. After the stress maximum, the composite shows a plateau effect, which could be caused by hardening of the alloy and/or by interlocking of the fracture surface.

4.3. In-situ tensile experiments

The stress–strain diagrams of the IMCC already show plasticity at low stress and flattens at higher elongation. The composite tends to a brittle fracture, which is illustrated by low toughness and sudden fracture. The graph suggests that the fracture behavior is dominated by the brittle ceramic and the brittle precipitates and plastic deformation is only initiated by the flattening of the curve before the maximum. The fracture behavior of the composite investigated by Kaveendran et al. also showed that the brittle Al_3Zr parties dominated the fracture mechanism [16].

The aluminum specimens have higher toughness due to unrestricted plasticity of the aluminum phase. The AR aluminum reached an ultimate tensile strength of 323 MPa. The IF aluminum was weakened due the slow cooling rate in the infiltration process and the coarsening of the primary silicon precipitations (compare Fig. 4). The material is overaged and the strength enhancement through the Orowan mechanism is worn off [27]. Prior to fracture, small stress drops were observed due to initial failure at the interfaces of the precipitates. The flattening of the stress–strain curve is explainable by the plastic deformation in the α -aluminum. When the stress dropped to 59 MPa, mainly the precipitates oriented perpendicular to the force direction fractured. However, since the precipitates are surrounded by the α -aluminum phase, complete failure does not occur. The α -phase initially bridges the crack by plastic deformation and is further deformed by increasing the strain.

The tensile behavior of the IMCC can be better analyzed by the recordings of the fractured specimen surface and the crack surface. The flattening of the curve after the linear elastic range is due to a plastic deformation or damage initiation in the metallic phase. In the curve shape of the plastic deformation the difference to the aluminum alloy is visible and shows, different mechanisms of plasticity are dominant in the materials. For the notched sample geometry, without an area of constant cross section (compare Fig. 2), the interpretation of absolute strain values until failure for the comparison of the metallic and composite sample is not possible. Cracking through the IMCC was perpendicular to the direction of force and could be attributed to three main areas, namely cracking at the interface, of the ceramic phase and of the precipitation in the metallic phase. The fracture direction and the mechanisms were also observed by several sources on other composites [1,18,19,44].

In addition to these mechanisms, crack branching as well as plastic deformation in the metallic phase were observed as shown in the EDX image. Further information can be provided by the investigation of the crack surfaces. The rough crack surface through the material and the pattern of the ceramic and metallic phase gets visible. The brittle fracture in ceramic phase and the precipitations can be seen in the SEM images in Fig. 13. The plastic deformation and the ductile fracture in α -aluminum is indicated in the dimples. The observations correlate well with the interpenetrating composite studied by Vecchina et al. [17] and further publications indicate similarities in the fractography [1,44]. By studying the fractured and polished surface in addition to the fracture surface during the in-situ SEM experiments, a detailed fractography could be performed and a good understanding of the relationship between microstructure and mechanical behavior could be provided.

5. Conclusion and outlook

Through in-situ SEM experiments, the tensile and compressive properties of the samples were recorded and analyzed using DIC. A novelty is that due to the microstructure of the composite, DIC was applied directly to the SEM images without the need for a speckle pattern. The microstructure analysis and DIC results are correlated with stress levels to provide detailed insight into damage behavior in interpenetrating metal-ceramic composites.

- The composite exhibited local pre-damage, which was attributed to the eigenstresses resulting from the metal solidification during manufacturing and due to the brittle precipitates.
- During compression experiments, defects in the aluminum-alumina composite showed an increase in size in the elastic range, and the observed stages of damage were similar to those reported by other researchers. Micro-cracks were observed in the ceramic phase that grew with increasing load, as well as plastic deformation of the metal phase and local debonding of the phase boundaries before the maximum strength was reached. The α -aluminum phase of the metal underwent plastic deformation, while the precipitates fractured. The material sheared at a 45° angle to the main loading direction, exhibited residual strength after fracture, and did not break into two parts because the energy was absorbed by the metal phase through plastic deformation.
- The microstructure was correlated with the damage behavior, taken into account the intermetallic phases and their contribution to the damage. These investigations revealed a further stage of damage, which emphasized the influence of the precipitates with the fracture behavior.
- DIC was used to quantify local strains to fracture, which were limited to the two diagonals at 45° to the main loading direction. The composite combines the stiffness of the ceramic phase with the plasticity of the aluminum alloy, resulting in an ultimate compression strength of up to 338 MPa and preventing total failure of the material. This property is crucial for construction materials, as it enables the prediction of total failure.
- In the tensile experiments, the IMCC exhibited a more brittle fracture behavior due to the dominant brittle nature of the ceramic and the precipitations under tension. The IMCC failed perpendicular to the direction of force, and in-situ SEM experiments allowed for a more detailed investigation of the fracture behavior, which was attributed to cracking at the interface, of the ceramic phase, and of the precipitations in the metallic phase. Crack branching as well as plastic deformation in the metallic phase were observed. The fracture pattern of the ceramic and metal phase was visible in the rough crack surface. All in all, the IMCC exhibits a good interface, as the crack growth occurred through the interface, the ceramic and the alloy.
- The slow cooling rate during the production of the composite influenced the microstructure and the mechanical properties, as evidenced by the alloy samples. Heat treatment of the microstructure could improve the mechanical properties under both tension and compression, as observed in microstructural investigations and in-situ SEM experiments.

CRediT authorship contribution statement

Philipp Christopher Morbitzer: Investigation, Writing – original draft. **Joél Schukraft:** Conceptualization, Writing – original draft. **Christoph Lohr:** Supervision, Writing – review & editing. **Kay André Weidenmann:** Project administration, Writing – review & editing.

Declaration of Competing Interest

The authors declare that they have no known competing financial interests or personal relationships that could have appeared to influence the work reported in this paper.

Data availability

Data will be made available on request.

Acknowledgements

The financial support of the German Research Foundation (DFG) within the project WE 4273/17-1 is gratefully acknowledged. We want

to thank Morgan Advanced Materials Haldenwanger GmbH for the friendly supply of complimentary preform material.

Data Availability Statement.

The raw/processed data required to reproduce these findings cannot be shared at this time as the data also forms part of an ongoing study.

References

- [1] Scherm F, Völkl R, Neubrand A, Bosbach F, Glatzel U. Mechanical characterisation of interpenetrating network metal-ceramic composites. *Mater Sci Eng A* 2010;527(4–5):1260–5. <https://doi.org/10.1016/j.msea.2009.09.063>.
- [2] Bodunrin MO, Alaneme KK, Chown LH. Aluminium matrix hybrid composites: a review of reinforcement philosophies; mechanical, corrosion and tribological characteristics. *J Mater Res Technol* 2015;4(4):434–45. <https://doi.org/10.1016/j.jmrt.2015.05.003>.
- [3] Clarke DR. Interpenetrating phase composites. *J Am Ceram Soc* 1992;75(4):739–58. <https://doi.org/10.1111/j.1151-2916.1992.tb04138.x>.
- [4] Mattern A, Huchler B, Staudenecker D, Oberacker R, Nagel A, Hoffmann MJ. Preparation of interpenetrating ceramic-metal composites. *J Eur Ceram Soc* 2004;24(12):3399–408. <https://doi.org/10.1016/j.jeurceramsoc.2003.10.030>.
- [5] O. Lavrentyeva, “Verfahren zur Herstellung von aufgeschäumten keramischen Werkstoffen sowie dadurch herstellbarer keramischer Schaum: DE,” DE102015202277A, 2015.
- [6] Schukraft J, Horny D, Schulz K, Weidenmann KA. 3D modeling and experimental investigation on the damage behavior of an interpenetrating metal ceramic composite (IMCC) under compression. *Mater Sci Eng A* 2022;844:143147. <https://doi.org/10.1016/j.msea.2022.143147>.
- [7] Kota N, Charan MS, Laha T, Roy S. Review on development of metal/ceramic interpenetrating phase composites and critical analysis of their properties. *Ceram Int* 2022;48(2):1451–83. <https://doi.org/10.1016/j.ceramint.2021.09.232>.
- [8] Mummareddy B, Maravola M, MacDonald E, Walker J, Hetzel B, Conner B, et al. The fracture properties of metal-ceramic composites manufactured via stereolithography. *Int J Appl Ceram Technol* 2020;17(2):413–23.
- [9] Roy S, Butz B, Wanner A. Damage evolution and domain-level anisotropy in metal/ceramic composites exhibiting lamellar microstructures. *Acta Materialia* 2010;58(7):2300–12. <https://doi.org/10.1016/j.actamat.2009.12.015>.
- [10] Roy S, Frohnheiser J, Wanner A. Effect of ceramic preform freeze-casting temperature and melt infiltration technique on the mechanical properties of a lamellar metal/ceramic composite. *J Compos Mater* 2020;54(15):2001–11. <https://doi.org/10.1177/0021998319890661>.
- [11] San Marchi C, Kouzeli M, Rao R, Lewis JA, Dunand DC. Alumina-aluminum interpenetrating-phase composites with three-dimensional periodic architecture. *Scripta Comput Sci Appl Math Materialia* 2003;49(9):861–6. [https://doi.org/10.1016/S1359-6462\(03\)00441-X](https://doi.org/10.1016/S1359-6462(03)00441-X).
- [12] Roy S, Gibmeier J, Kostov V, Weidenmann KA, Nagel A, Wanner A. Internal load transfer in a metal matrix composite with a three-dimensional interpenetrating structure. *Acta Materialia* 2011;59(4):1424–35. <https://doi.org/10.1016/j.actamat.2010.11.004>.
- [13] Roy S, Gibmeier J, Kostov V, Weidenmann KA, Nagel A, Wanner A. Internal load transfer and damage evolution in a 3D interpenetrating metal/ceramic composite. *Mater Sci Eng A* 2012;551:272–9. <https://doi.org/10.1016/j.msea.2012.05.016>.
- [14] Wang F, Zhang X, Wang Y, Fan Q, Li G. Damage evolution and distribution of interpenetrating phase composites under dynamic loading. *Ceram Int* 2014;40(8):13241–8. <https://doi.org/10.1016/j.ceramint.2014.05.031>.
- [15] Li G, Zhang Xu, Fan Q, Wang L, Zhang H, Wang F, et al. Simulation of damage and failure processes of interpenetrating SiC/Al composites subjected to dynamic compressive loading. *Acta Materialia* 2014;78:190–202.
- [16] Kaveendran B, Wang GS, Huang LJ, Geng L, Peng HX. In situ (Al₃Zr+Al₂O₃np)/2024Al metal matrix composite with novel reinforcement distributions fabricated by reaction hot pressing. *J Alloy Compd* 2013;581:16–22. <https://doi.org/10.1016/j.jallcom.2013.06.143>.
- [17] Vecchia GM, Badini C, Puppo D, D’Errico F. Co-continuous Al/Al₂O₃ composite produced by liquid displacement reaction: relationship between microstructure and mechanical behavior. *J. Mater. Sci.* 2003;38(17):3567–77. <https://doi.org/10.1023/A:1025613011787>.
- [18] Srivatsan TS, Al-Hajri M, Smith C, Petraroli M. The tensile response and fracture behavior of 2009 aluminum alloy metal matrix composite. *Mater. Sci. Eng. A* 2003;346(1–2):91–100. [https://doi.org/10.1016/S0921-5093\(02\)00481-1](https://doi.org/10.1016/S0921-5093(02)00481-1).
- [19] Zhou W, Hu W, Zhang Di. Metal-matrix interpenetrating phase composite and its in situ fracture observation. *Mater Lett* 1999;40(4):156–60. [https://doi.org/10.1016/S0167-577X\(99\)00067-1](https://doi.org/10.1016/S0167-577X(99)00067-1).
- [20] Horny D, Schukraft J, Weidenmann KA, Schulz K. Numerical and experimental characterization of elastic properties of a novel, highly homogeneous interpenetrating metal ceramic composite. *Adv Eng Mater* 2020;22(7):1901556. <https://doi.org/10.1002/adem.201901556>.
- [21] D. Wegscheider, J. Schukraft, and K. Weidenmann, “A metallographic preparation routine for an AlSi10Mg-Al₂O₃ interpenetrating composite,” in *Metallographie 2022*, Saarbrücken, DGM e.V., Ed., 2022.
- [22] Schukraft J, Lohr C, Weidenmann KA. 2D and 3D in-situ mechanical testing of an interpenetrating metal ceramic composite consisting of a slurry-based ceramic foam and AlSi10Mg. *Compos Struct* 2021;263:113742. <https://doi.org/10.1016/j.compstruct.2021.113742>.
- [23] Schukraft J, Lohr C, Weidenmann KA. Approaches to X-ray CT evaluation of in-situ experiments on damage evolution in an interpenetrating metal-ceramic composite with residual porosity. *Appl Compos Mater* 2023;30(3):815–31.
- [24] Basista M, Jakubowska J, Węglewski W. Processing induced flaws in aluminum-alumina interpenetrating phase composites. *Adv Eng Mater* 2017;19(12):1700484. <https://doi.org/10.1002/adem.201700484>.
- [25] Bociaga E, Jaruga T. “Visualization of melt flow lines in injection moulding”. *J Achievements of Mater Manuf Engi* 2006;18:1–2.
- [26] Iilschner B, Singer RF. *Werkstoffwissenschaften und fertigungstechnik: eigenschaften, vorgänge, technologien*. 5th ed. (Springer-Lehrbuch). Berlin and Heidelberg: Springer; 2010.
- [27] Bargel H-J, Schulze G, editors. *Werkstoffkunde*. Berlin, Heidelberg: Springer Berlin Heidelberg; 2008.
- [28] Dobkowska A, Adamczyk – Cieślak B, Mizera J, Kurzydowski KJ, Kielbus A. The comparison of the microstructure and corrosion resistance of sand cast aluminum alloys. *Arch Metall Mater* 2016;61(1):209–12.
- [29] Hadadzadeh A, Amirkhiz BS, Mohammadi M. Contribution of Mg₂Si precipitates to the strength of direct metal laser sintered AlSi10Mg. *Mater Sci Eng A* 2019;739:295–300. <https://doi.org/10.1016/j.msea.2018.10.055>.
- [30] Kempen K, Thijs L, van Humbeeck J, Kruth JP. Mechanical properties of AlSi10Mg produced by selective laser melting. *Physics Procedia* 2012;39:439–46. <https://doi.org/10.1016/j.phpro.2012.10.059>.
- [31] Zhou Le, Mehta A, Schulz E, McWilliams B, Cho K, Sohn Y. Microstructure, precipitates and hardness of selectively laser melted AlSi10Mg alloy before and after heat treatment. *Mater Charact* 2018;143:5–17.
- [32] Aboulkhair NT, Tuck C, Ashcroft I, Maskery I, Everitt NM. On the precipitation hardening of selective laser melted AlSi10Mg. *Metallurgical and Mater Trans A* 2015;46(8):3337–41. <https://doi.org/10.1007/s11661-015-2980-7>.
- [33] Bösch D, Pogatscher S, Hummel M, Fragner W, Uggowitzer PJ, Göken M, et al. Secondary Al-Si-Mg high-pressure die casting alloys with enhanced ductility. *Metall Mater Trans A* 2015;46(3):1035–45.
- [34] M. Voncina, P. Mrvar, and J. Medved, *Thermodynamic Analysis of AlSi10Mg Alloy* (52), 2006.
- [35] Sobczak N, Ksiazek M, Radziwill W, Asthana R, Mikulowski B. The effect of temperature, matrix alloying and substrate coatings on wettability and shear strength of Al/Al₂O₃ couples. *Metall Mater Trans A* 2004;35(3):911–23. <https://doi.org/10.1007/s11661-004-0016-9>.
- [36] Takata N, Kodaira H, Sekizawa K, Suzuki A, Kobashi M. Change in microstructure of selectively laser melted AlSi10Mg alloy with heat treatments. *Mater Sci Eng A* 2017;704:218–28. <https://doi.org/10.1016/j.msea.2017.08.029>.
- [37] D. Stefanescu and R. Ruxanda, “Solidification Structure of Aluminum Alloys,” in *ASM Handbook vol. 9 - Metallography and Microstructures*, 2004, pp. 107–115.
- [38] Neuser M, Grydin O, Frolov Y, Schaper M. Influence of solidification rates and heat treatment on the mechanical performance and joinability of the cast aluminium alloy AlSi10Mg. *Prod Eng* 2022;16(2–3):193–202. <https://doi.org/10.1007/s11740-022-01106-1>.
- [39] Cai C, Geng H, Wang S, Gong B, Zhang Z. Microstructure evolution of AlSi10Mg (Cu) alloy related to isothermal exposure. *Materials* 2018;11(5):809. <https://doi.org/10.3390/ma11050809>.
- [40] Schukraft J, Lohr C, Weidenmann KA. Mechanical characterization of an interpenetrating metal-matrix composite based on highly homogeneous ceramic foams. In: Hausmann JM, Siebert M, von Hehl A, Weidenmann KA, editors. *Hybrid 2020 Materials and Structures*. Sankt Augustin; 2020. p. 33–9.
- [41] Wang L, Fan Q, Li G, Zhang H, Wang F. Experimental observation and numerical simulation of SiC₃D/Al interpenetrating phase composite material subjected to a three-point bending load. *Comput Mater Sci* 2014;95:408–13. <https://doi.org/10.1016/j.commatsci.2014.08.008>.
- [42] Chang H, Binner J, Higginson R, Myers P, Webb P, King G. High strain rate characteristics of 3–3 metal-ceramic interpenetrating composites. *Mater Sci Eng A* 2011;528(6):2239–45. <https://doi.org/10.1016/j.msea.2010.12.016>.
- [43] Bandyopadhyay A, Atisivan R, Kuhn G, Yeruva S. Mechanical properties of interconnected phase alumina-Al composites 24. The University of Texas at Austin; 2000.
- [44] Ceschini L, Minak G, Morri A. Forging of the AA2618/20vol.% Al₂O₃p composite: effects on microstructure and tensile properties. *Compos Sci Technol* 2009;69(11–12):1783–9. <https://doi.org/10.1016/j.compscitech.2008.08.027>.